Journal of Alloys and Compounds 509 (2011) 10139–10144

Contents lists available at SciVerse ScienceDirect

Journal of Alloys and Compounds

journal homepage: www.elsevier.com/locate/jallcom

Phase pure synthesis of $BiFeO_3$ nanopowders using diverse precursor via co-precipitation method

M. Yasin Shami[a,*], M.S. Awan[b], M. Anis-ur-Rehman[a]

[a] *Applied Thermal Physics Laboratory, Department of Physics, COMSATS Institute of Information Technology, Park Road, Islamabad 44000, Pakistan*
[b] *Center for Micro and Nano Devices, Department of Physics, COMSATS Institute of Information Technology, Park Road, Islamabad 44000, Pakistan*

ARTICLE INFO

Article history:
Received 6 May 2011
Received in revised form 11 August 2011
Accepted 12 August 2011
Available online 22 August 2011

Keywords:
Multiferroics
$BiFeO_3$
Iso-static pressing
Transition temperature
Phase stoichiometry
Polarization

ABSTRACT

Amorphous powder of $BiFeO_3$ (BFO) was synthesized at low-temperature (80 °C) by co-precipitation method. Optimal synthesis conditions for phase pure BFO were obtained. Powders were calcined in the temperature range from 400 to 600 °C for 1 h. Iso-statically pressed powder was sintered at 500 °C for 2 h. Differential scanning calorimetric thermo-gram guided for phase transition, crystallization and melting temperatures. X-ray diffraction confirmed the amorphous nature of as synthesized powder and phase formation of calcined powders. Calcination at temperature ≥400 °C resulted in nano crystalline powders with perovskite structure. Average crystallite size increased with the increase in calcination temperature. Scanning electron microscopic studies revealed dense granular microstructure of the sintered samples. The sintered samples exhibited high dc resistivity at room temperature which decreased with the increase in temperature. Dielectric constant, dielectric loss tangent and ac conductivity measurements were carried out in the frequency range (10 Hz to 2 MHz). The samples responded weak electric and magnetic polarization at room temperature with unsaturated and hysteresis free loops, respectively.

© 2011 Elsevier B.V. All rights reserved.

1. Introduction

The study of multiferroic materials is of great interest because they exhibit more than one ferroic order parameters (ferroelectricity, ferromagnetism, and ferroelasticity) in the same phase [1]. These materials are under significant investigation due to the fascinating fundamental physics and mesmerizing applications. Ferromagnetism hardly coexist with other ferroic orders (ferroelectricity) due to their structural competition because the 3d electrons, which are essential for magnetism, reduce the tendency for off-center ferroelectric distortion [2]. Such systems are rare in nature and examples can be found in perovskite oxides like: $BiFeO_3$, $BiMnO_3$ and $YMnO_3$. BFO has received much more attention nowadays due to its multiferroicity at room temperature [3]. It is anticipated that such materials will be the basis of next generation devices, due to the intrinsic coupling between the electric polarization and magnetic moment, that could, in principle, permit data to be written electrically and then read magnetically [4]. Other fascinating applications can be found in spintronic devices, sensors, multiple state memory elements, electrically controllable ferromagnetic resonance devices and transducers with magnetically modulated piezoelectricity [5].

BFO possesses simultaneously ferroelectric phase with the Curie temperature ($T_C = 827\,°C$) and G-type antiferromagnetic order with Néel temperature ($T_N = 370\,°C$). It has distorted perovskite pseudocubic structure with space group R3c [6]. Its crystal can be seen either as a rhombohedral unit cell or as hexagonal unit cell. Two distorted perovskite cells connected through the body diagonal form a rhombohedral unit cell whereas the hexagonal cell consists of six formula units. The cations are displaced from their symmetric positions relative to the anions along the [1 1 1] direction. The oxygen octahedral is rotated clockwise and anticlockwise around the [1 1 1] direction alternately. It has cycloidal spin structure with a period of 62 nm. This spin has been found incommensurate with structural lattice and ultimately exhibiting a weak ferromagnetism at room temperature [7]. The energy of the BFO structure can be lowered by off-center the Bi ion with respect to its oxygen ions which leads to a hybridization of both Bi 6s and 6p states with O 2p orbitals. This led to a displacement of Bi cation relative to $Fe–O_6$ octahedral which causes the intrinsic electric polarization [2].

Although BFO was discovered in late 1950s [8], its application in the industry was hampered due to difficulties in its phase pure synthesis. Impurity phases like Bi_2O_3, $Bi_2Fe_4O_9$ (mullite) and $Bi_{25}FeO_{39}$ (sillenite) are formed during its synthesis. These phases change its stoichiometry and create oxygen vacancies. Also during the processing oxidation state of iron may change which results in leakage currents that are not desirable for practical usage [3].

---

* Corresponding author. Tel.: +92 3325157527.
E-mail address: m_yasin_shami@yahoo.com (M.Y. Shami).

0925-8388/$ – see front matter © 2011 Elsevier B.V. All rights reserved.
doi:10.1016/j.jallcom.2011.08.063

Synthesis of phase pure BFO is rather difficult due to the kinetic and thermodynamic properties of the Bi_2O_3–Fe_2O_3 system [9]. BFO nanopowders can be synthesized by wet chemical methods like: (sol gel, auto combustion, solvothermal and co-precipitation) and solid state reaction. The main purpose behind each synthesis technique is to obtain the highest purity at the lowest possible temperature with a simple recipe to make it cost effective for industrial applications. In the solid state method, oxides are reacted at temperature above 800 °C and extra phases are removed by leaching with HNO_3 [10]. Disadvantages of this process are coarser powder, extra phases and poor reproducibility. Nano sized BFO powder can be obtained by sol gel [11] and auto combustion [12] but these methods involve complex solutions and toxic reactions. Navarro et al. [13] reported a new method for synthesizing BFO by thermal decomposition of $Bi[Fe(CN)_6]{\cdot}4H_2O$ but could not avoid impurities like Bi_2O_3, Fe_2O_3 and $(BiO)_2CO_3$. Synthesis by solvothermal has shown good results for tailoring the morphology of BFO grains [14]. Co-precipitation is, in general, a cheap and simple method, with the main advantage of significantly lower synthesizing temperature than the above mentioned methods. But the formation of impure phases, keep the researcher away from adopting this method. Recently Ke et al. [9] have controlled different processing factors for the synthesis of BFO by the co-precipitation method but could not get rid of the impure phases.

Traditionally in co-precipitation, nitrates of bismuth and iron are being used as precursors but in this work, we have used bismuth oxide (Bi_2O_3) and iron nitrate ($Fe(NO_3)_3{\cdot}9H_2O$) as precursors. Phase pure BFO nanopowders have been synthesized at a considerably low temperature (400 °C). Effects of calcination temperature on crystallinity, phase formation and microstructure have been studied systematically. Characterizations were conducted on powders and iso-statically pressed sintered pellets.

2. Experimental

2.1. Synthesis of $BiFeO_3$

Amorphous powder of multiferroic BFO has successfully been synthesized by a cost effective co-precipitation route at low temperature (80 °C). The analytical grade iron nitrate nonahydrate $Fe(NO_3)_3{\cdot}9H_2O$ and commercial grade bismuth oxide Bi_2O_3 (99.98% pure) were used as precursors. These were dissolved in nitric acid (HNO_3) and deionized water to form solutions of 0.4 M. Both the solutions were mixed and stirred for 30 min to obtain a uniform transparent ionic mixture. An aqueous solution of sodium hydroxide (NaOH) prepared in deionized water of 1.0 M was used as a precipitating agent. It was mixed quickly into the ionic solution during stirring on a hot plate heater to form uniform precipitates. For phase-purity and desired crystallite size, a value of pH = 12 was maintained at 30 °C [15]. After vigorous stirring for 30 min, the temperature of the solution was raised to 80 ± 2 °C and kept it for 45 min to transform hydroxides into ferrite. The solution thus obtained was washed successively with deionized water till a pH of 7 was achieved. The precipitates thus obtained were dried in an electric oven at 100 °C. Dried chunks were ground in a mortar and pestle to obtain an amorphous powder. For crystallization and phase formation, powder was calcined at different temperatures (400–600) °C for 1 h with a step of 50 °C. For other characterization, powder was uniaxially pressed at a pressure of 10 MPa into green pellets. These pellets were further densified by cold iso-static pressing at 250 MPa and sintered at 500 °C for 2 h. All the heat treatments were carried out in the air.

2.2. Characterization

The structural analysis and phase composition of the powders were determined using X-ray diffractometer (XRD) (PANalytical, X'Pert Pro) with Cu Kα radiation source and operated at 40 kV and 30 mA. The grain size and morphology were observed using scanning electron microscope (SEM) (HITACHI SU-1500) equipped with energy dispersive X-ray spectroscopy (EDX). Thermal analysis of the powder was performed using differential scanning calorimetry (DSC) (STA409C, NETZCH, Germany). The dielectric data was collected in the frequency range from 10 Hz to 2 MHz by using QuadTech 7600 LCR Analyzer at room temperature. Electrical dc resistivity of the sintered sample was measured on (DCM350) from room temperature up to 300 °C. Magnetic properties were performed on dc magnetometer (Riken Denshi Co Ltd., Japan). Ferroelectric measurements were made on ferroelectric tester and Keithley (8512A) electrometer.

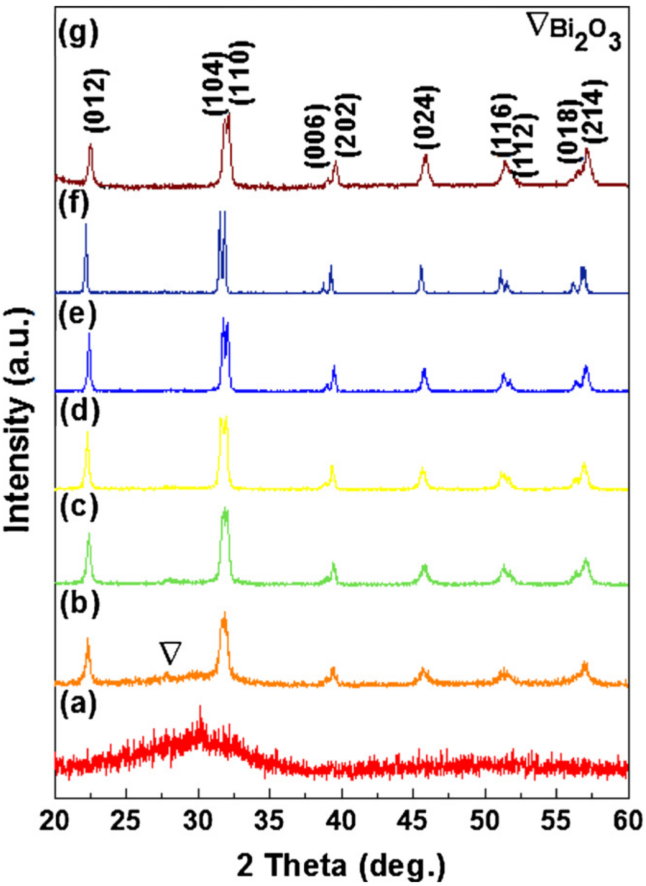

Fig. 1. XRD patterns of $BiFeO_3$ (a) as synthesized powder, then calcined powders in the air for 1 h at (b) 400 °C, (c) 450 °C, (d) 500 °C, (e) 550 °C, (f) 600 °C and (g) pellet sintered in air at 500 °C for 2 h. Peaks labeled with JCPD card No. 01-072-7678.

3. Results and discussion

3.1. Synthesis analysis

In co-precipitation method, nitrates of bismuth and iron are being used normally as precursors for the synthesis of BFO [9]. In the present work, we have used bismuth oxide (Bi_2O_3) and iron nitrate ($Fe(NO_3)_3{\cdot}9H_2O$) as precursors. Iron nitrate nonahydrate ($Fe(NO_3)_3{\cdot}9H_2O$) is soluble in deionized water but bismuth nitrate pentahydrate ($Bi(NO_3)_3{\cdot}5H_2O$) and bismuth oxide (Bi_2O_3) require acid to dissolve. It was observed experimentally that almost three times more nitric acid (HNO_3) is required to dissolve bismuth nitrate than bismuth oxide. Ultimately more precipitating agent (NaOH/KOH) and mixing time is required to complete the ferritization process. These factors might be responsible for the formation of extra phases like $Bi_2Fe_4O_{19}$ and $Bi_{25}FeO_{39}$ [9,16].

3.2. Structural properties

Phase formation and crystallite size of the BFO powders were determined from the XRD analysis. Fig. 1 shows XRD patterns of the as synthesized, calcined and sintered BFO samples. It is confirmed that as synthesized powder was amorphous in nature as shown in Fig. 1(a). The crystalline peaks were absent in the entire (2θ) range. The powder crystallized at a temperature, as low as 400 °C, this is shown in Fig. 1(b). Further increase in calcination temperature up to 600 °C, improved the crystallinity of BFO powders. The powder calcined at 400 °C contains a minor peak of Bi_2O_3, which diminished at higher temperature. Fig. 1(g) shows the XRD pattern of

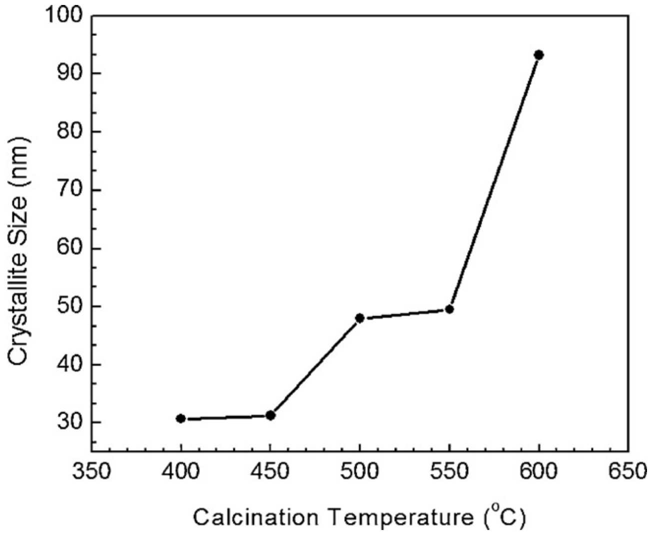

Fig. 2. Crystallite size of $BiFeO_3$ powder as a function of calcination temperature.

the BFO pellet sintered at 500 °C/2 h. All the peaks were labeled by comparing XRD data with the JCPD card No. 01-072-7678. BFO exhibited rhombohedral R3c crystal structure. The lattice parameters and unit cell volume of the sintered samples were calculated using chekcell software (Developed at Laboratory des Matériaux et du Génie Physique, Ecole Nationale Supérieure de Physique de Grenoble (INPG), Domaine Universitaire BP 46, 38402 Saint Martin d'Hères, France). The obtained values are $a = 5.58$ Å, $c = 13.89$ Å and volume = 375 Å^3. These parameters are in good accordance with the literature [17]. Different calcination temperatures did not show any significant effect on the lattice parameters. The crystallite sizes of calcined powders were calculated using the Scherrer formula:

$$t = \frac{0.9\lambda}{\beta\cos(\theta_B)} \tag{1}$$

where t is the crystallite size, λ is the wavelength of incident X-rays ($\lambda = 1.5406$ Å), β is the diffraction angle and β is the full width at half maximum (FWHM). The two major peaks (1 0 4) and (1 1 0) were used for the calculations. Fig. 2 shows the crystallite size of the powder as a function of calcination temperatures. It is evident that the average crystallite size increased (31–93) nm with the increase in calcination temperature. The porosity of the sintered pellet was determined using the formula [18]

$$P = 1 - \left(\frac{\rho_m}{\rho_t}\right) \tag{2}$$

where ρ_m and ρ_t are the measured density and theoretical density. The density ($\rho_m = 7.13$ g/cm^3) was measured using Archimedes method. The theoretical density ($\rho_t = 8.41$ g/cm^3) was calculated using the following formula

$$\rho_t = \left(\frac{nM}{VN_A}\right) \tag{3}$$

where n is the number of formula units in BFO hexagonal unit, M is the molecular mass of one formula unit, V is the volume of unit cell and N_A is the Avogadro's number. The calculated value of porosity of the sample sintered at 500 °C/2 h was ($P = 0.15$). This value is considerably low which might be due to cold iso-static pressing of pellets.

3.3. Morphology

The particle size/distribution, morphology and chemical analysis of the powders were carried out using SEM equipped with the EDX system. Fig. 3 illustrates the SEM micrographs of the BFO powders calcined at different temperatures in the range from 400 to 600 °C. To analyze, powders were loosely spread on the carbon tapes as shown in the inset (low magnification view) of Fig. 3(a). The powder particles were aggregated into clusters in the range of several hundred nanometers. The powder calcined at 400 °C consists of fine fluffy clusters as shown in Fig. 3(a). Magnified view of the circled (dashed) cluster in the inset is shown in Fig. 3(a). BFO powders calcined at 550 °C and 600 °C revealed granular microstructure as shown in Fig. 3(b) and (c). The micrographs of calcined powder at 550 °C exhibited an average particle size around 200 nm. Whereas the powder calcined at 600 °C has an average particle size in the range of (100–500) nm. This showed that reaction products (calcined powders) consist of broad particle sized distribution and the average particle size increased with the increase in calcinations temperature. Fig. 3(d) shows the fractured surface SEM micrograph of the iso-statically pressed BFO sample sintered at 500 °C/2 h. The average grain size lies between 200 and 250 nm. The micrograph revealed narrow particle size distribution and dense microstructure. Ferroelectric grains are well connected with each other. This is necessary for better electrical properties.

3.4. Thermal analysis

Thermal stability, phase transformation, crystallization temperatures and melting point of as synthesized powder were determined by the high temperature differential scanning calorimetric (DSC) studies. The sample was scanned from room temperature to 1000 °C at a heating rate of 10 °C/min using empty crucible of Al_2O_3 as reference material. Measurements were carried out under the dynamic atmosphere of inert (Ar) gas. Fig. 4 is the DSC thermo-gram of as synthesized BFO powder which was amorphous in nature as confirmed in the XRD pattern (Fig. 1(a)). The powder showed a broad exothermic response in the entire temperature range. This consists of one exothermic and three endothermic features. The peak around 466.3 ± 1 °C corresponds to the crystallization of amorphous powder [9], which is also confirmed in the XRD pattern as shown in Fig. 1(b)–(g). There are two sharp endothermic peaks at 802.4 ± 1 °C and 816.2 ± 1 °C which corresponds to the ferroelectric to paraelectric phase transformation temperature and melting of Bi_2O_3, respectively [19]. Finally there is a sharp endothermic peak at 969.2 ± 1 °C which corresponds to the heat loss at the melting point of BFO ceramics which is in good agreement with the literature [14].

3.5. Electrical dc resistivity

Electrical dc resistivity (ρ) measurements were carried out using two probe method [17,20] from room temperature to 300 °C. Disc shaped pellet of approximately 6 mm diameter and 2 mm thickness was used for these measurements. Pressure contacts equal to the pellet size were used after polishing the surfaces. Resistivity measured at room temperature was 0.45 GΩ-cm which decreased with the increase in temperature. This semiconducting behavior of the sample may be due to the transport mechanism of polarons, thermally activated electrons to the conduction band and thermally assisted tunneling of charge carriers through grain boundaries [17]. Activation energy was calculated from slop of the linear plot of $\ln(\rho)$ vs reciprocal of k_BT as shown in Fig. 5 using Arrhenius relation [21,22]

$$\rho = \rho_o \exp\left(\frac{E_a}{k_BT}\right) \tag{4}$$

where ρ is the resistivity at temperature T, ρ_o is the temperature independent constant, E_a is activation energy corresponding

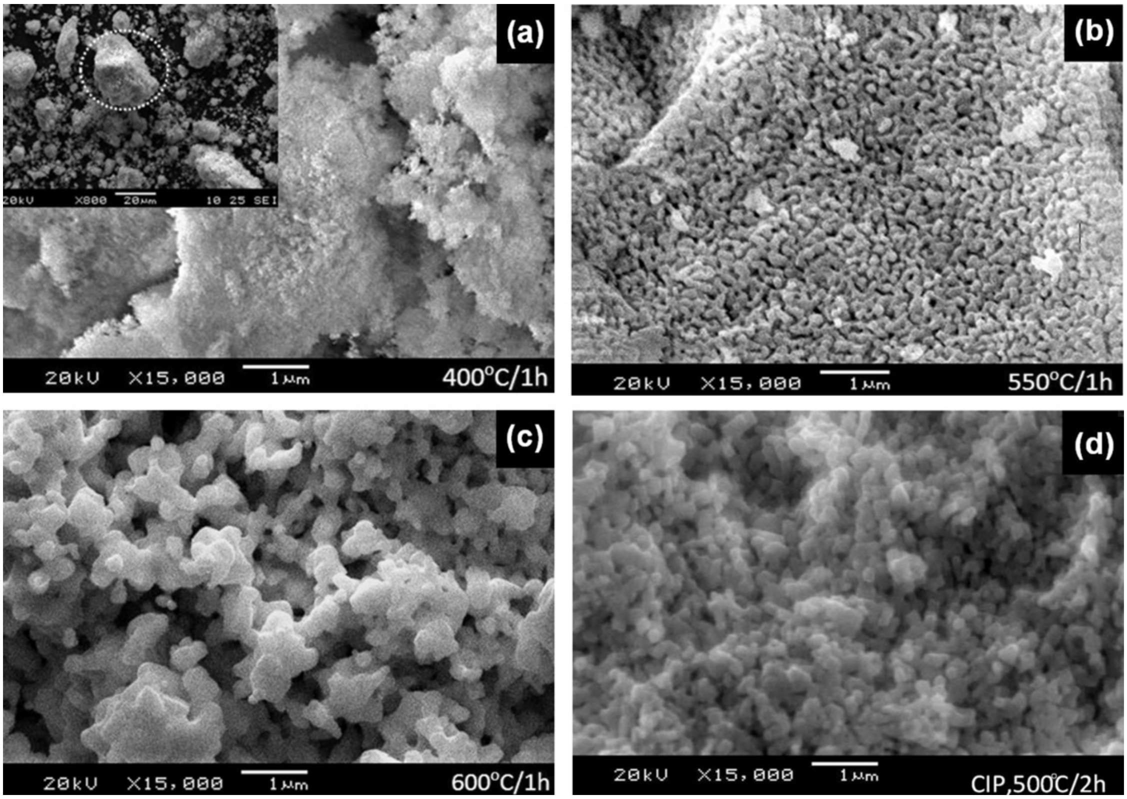

Fig. 3. SEM micrographs of $BiFeO_3$ powders calcined for 1 h at (a) 400 °C, (b) 550 °C, (c) 600 °C and (d) pellet sintered at 500 °C for 2 h. Inset (a) shows the features at low magnification.

to electrical process and k_B is the Boltzmann's constant. The value of activation energy for BFO sample is 0.628(9) eV.

3.6. Dielectric properties

The dielectric loss tangent (tan(δ)), dielectric constant ($\acute{\varepsilon}$) and ac conductivity (σ_{ac}) of the sintered (BFO) sample were measured in the frequency range from 10 Hz to 2 MHz as shown in Fig. 6. Measurements were conducted at room temperature by parallel plate technique. Two dielectric relaxation peaks at 23 Hz and 250 kHz can be observed in dielectric loss tangent as shown in Fig. 6(a). At low frequencies the space charges are able to follow the applied field but at high frequencies these space charges have not sufficient time to build up and undergo relaxation. So dielectric relaxation at low frequencies can be ascribed to the grain and grain boundary structures whereas dielectric relaxation behavior at high frequencies can be attributed to the valance fluctuation of Fe ions [23]. The dielectric constant ($\acute{\varepsilon}$) was calculated by the following relation

$$\acute{\varepsilon} = \frac{C\,d}{\varepsilon_o A} \tag{5}$$

where d is the thickness of pellet, C is the capacitance, ε_o is the permittivity of free space and A is the cross-sectional area of the pellet. The dielectric constant ($\acute{\varepsilon}$) behavior of the sample in the frequency

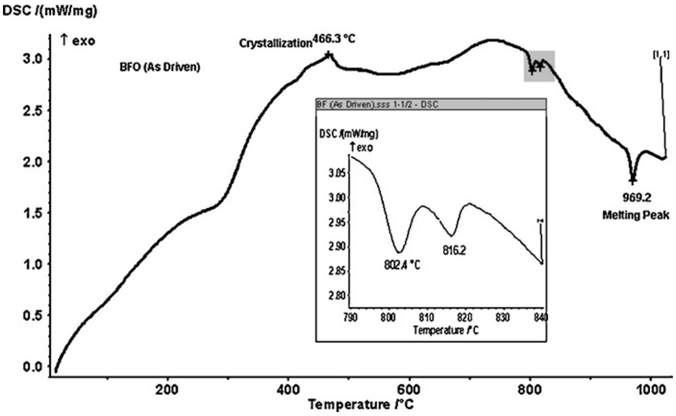

Fig. 4. DSC thermogram of the as-synthesized $BiFeO_3$ powder. Inset shows the enlarged view of the selected area.

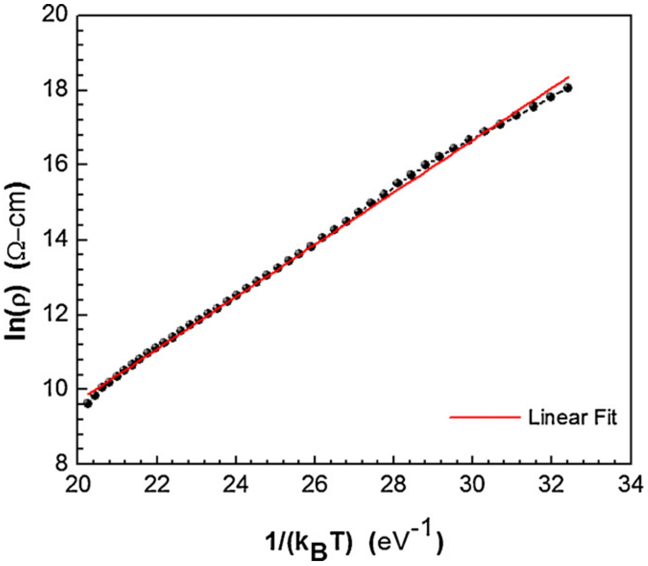

Fig. 5. Plots of dc measurements showing log of resistivity as a function of $1/(k_BT)$. Solid line is a linear fit of the graph to measure the slope.

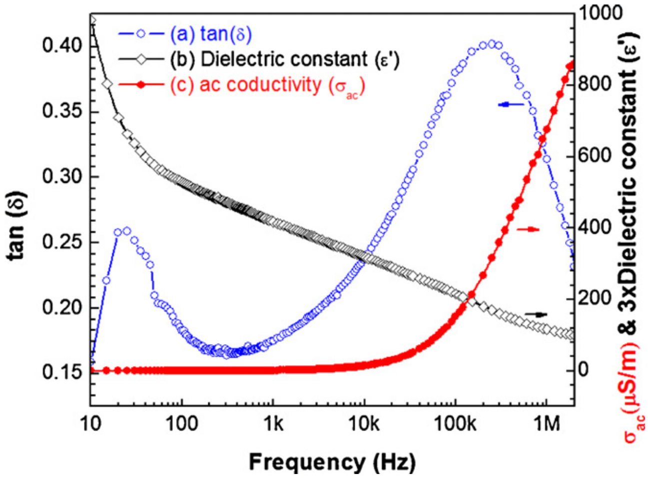

Fig. 6. Graphs of ac measurements as a function of frequency from 10 Hz to 2 MHz. (a) Dielectric loss tangent (tan δ), (b) dielectric constant $\acute{\varepsilon}$ and (c) ac conductivity σ_{ac}.

range (10 Hz to 2 MHz) can be observed in Fig. 6(b). Decrease in dielectric constant is abrupt from 10 Hz to 50 Hz and afterwards it varies gradually up to 2 MHz. It seems that the effect of interfacial polarization at low frequencies diminishes slowly before the domination of dipole polarization at high frequencies. This dielectric behavior can be inferred from Maxwell–Wagner interfacial type polarization [24].

The ac conductivity was also evaluated from dielectric constant ($\acute{\varepsilon}$) and dielectric loss tangent (tan(δ)) in the same frequency range mentioned above using the following relation [18]

$$\sigma_{ac} = \omega\varepsilon_o\dot{\varepsilon}\tan(\delta) \tag{6}$$

where σ_{ac} is the ac conductivity, ω is the angular frequency. It can be observed from Fig. 6(c) that σ_{ac} increases with the increase in frequency which is in accordance with the Maxwell–Wagner model [24].

3.7. Magnetization

The magnetic measurements of BFO samples were carried out at room temperature on a cylindrical shaped pellet sintered at 500 °C for 2 h. Fig. 7 shows the magnetization as a function of applied magnetic field, whereas the inset shows the selected area magnified view of Fig. 7 at low applied field (±0.05 T). The magnetic loop follows almost linear field-dependence of magnetization and an unsaturated hysteresis loop was observed. This is an indication of anti-ferromagnetic (AF) order at room temperature [9]. The anti-ferromagnetism is developed due to super exchange interactions between the Fe ions which occupy the sites of octahedral and tetrahedral coordination [14]. Weak ferromagnetism at room temperature with a remnant magnetization (Mr ~ 3.8 × 10^{-4} emu/g) and coercive field (Hc ~ 14.6 × 10^{-4} T) was observed in the M-H loop. This weak magnetism is a bit different from that of bulk BFO [25]. This might be due to canting of the antiferromagnetic spin structure and due to the size effect. Particles at nano scale exhibit significantly different properties as compared to the bulk. With the decrease in particle size, surface-to-volume ratio becomes large and long range antiferromagnetic order is frequently interrupted at the surfaces. The contribution of uncompensated spins at the surface to the total magnetic moment of the particle increases. An intrinsic spiral spin structure is partially suppressed which lead to weak ferromagnetism of the nano particles [26]. Magnetization may also be induced by spin canting or structural distortion in BFO [27]. Spins are coupled via a Fe^{3+}–O^{2-}–Fe^{3+} super exchange mechanism.

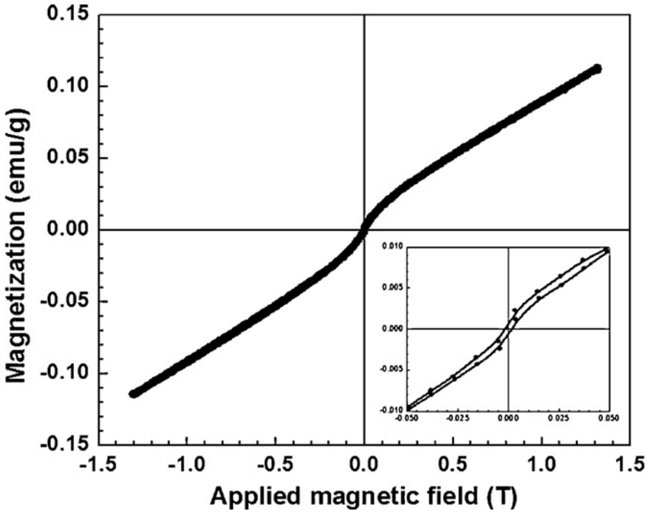

Fig. 7. M–H loop of the $BiFeO_3$ sample sintered at 500 °C for 2 h in the air. Inset shows partially enlarged view of the selected area.

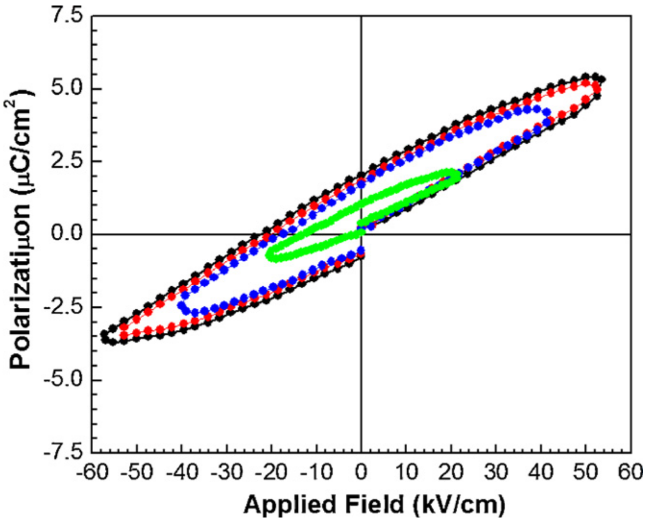

Fig. 8. P–E loops of $BiFeO_3$ pellet with different applied electric fields.

3.8. Ferroelectricity

Ferroelectric behavior of the sample was investigated at room temperature using a thin disc shaped pellet sintered at 500 °C for 2 h. Polarization vs electrical field (P-E) loops in Fig. 8 showed the ferroelectric nature of the sample. Maximum polarization P_m = 5.49 μC/cm^2, remnant polarization 2P_r = 2.8 μC/cm^2 and coercive field E_c = 23.9 kV/cm were observed. P-E loops were not saturated due to high electrical losses which may be related to a number of structural defects, domains with different orientation, grain boundaries and oxygen vacancies [28].

4. Conclusions

Phase pure multiferroic $BiFeO_3$ nanopowder has been synthesized by simple co-precipitation method at a temperature, as low as 400 °C. Precursor Bi_2O_3 played an important role in avoiding the impure phases. Pure phase of BFO has been confirmed by XRD analysis. Crystallite and grain size increased with the increase in calcination temperature. Sintered samples showed dielectric constant of (328) for low frequency at room temperature. SEM micrograph showed granular microstructure which agglomerated with the increase of calcination temperature. Ferroelectric to paraelectric phase transformation was observed at $816 \pm 1\,^{\circ}\mathrm{C}$. The sample showed remnant magnetization (Mr $\sim 3.8 \times 10^{-4}$ emu/g) and coercive field (Hc $\sim 14.6 \times 10^{-4}$ T) at room temperature. This weak magnetization in pure BFO can be improved either by using dopants or synthesizing its composites. Maximum polarization ($P_{\mathrm{m}} = 5.49\ \mu\mathrm{C/cm^2}$) and remnant polarization ($2P_{\mathrm{r}} = 2.8\ \mu\mathrm{C/cm^2}$) were projected from the unsaturated ferroelectric hysteresis loop.

References

[1] N.V. Minh, N.G. Quan, J. Alloys Compd. 509 (2011) 2663–2666.
[2] X. Zhang, Y. Sui, X. Wang, J. Mao, R. Zhu, Y. Wang, Z. Wang, Y. Liu, W. Liu, J. Alloys Compd. 509 (2011) 5908–5912.
[3] X. Zhang, Y. Sui, X. Wang, Y. Wang, Z. Wang, J. Alloys Compd. 507 (2010) 157–161.
[4] K. Liu, H. Fan, P. Ren, C. Yang, J. Alloys Compd. 509 (2011) 1901–1905.
[5] S.K. Pradhan, J. Das, P.P. Rout, S.K. Das, S. Samantray, D.K. Mishra, D.R. Sahu, A.K. Pradhan, K. Zhang, V.V. Srinivasu, B.K. Roul, J. Alloys Compd. 509 (2011) 2645–2649.
[6] D. Varshney, A. Kumar, K. Verma, J. Alloys Compd. 509 (2011) 8421–8426.
[7] Q. Xu, X. Zheng, Z. Wen, Y. Yang, D. Wu, M. Xu, Solid State Commun. 151 (2011) 624–627.
[8] L.W. Martin, Y.H. Chu, R. Ramesh, Mater. Sci. Eng. R 68 (2010) 89–133.
[9] H. Ke, W. Wang, Y. Wang, J. Xu, D. Jia, Z. Lu, Y. Zhou, J. Alloys Compd. 509 (2011) 2192–2197.
[10] M. Awan, A. Bhatti, J. Mater. Eng. Perform. 20 (2011) 283–288.
[11] V.S. Puli, A. Kumar, N. Panwar, I.C. Panwar, R.S. Katiyar, J. Alloys Compd. 509 (2011) 8223–8227.
[12] J. Yang, X. Li, J. Zhou, Y. Tang, Y. Zhang, Y. Li, J. Alloys Compd. 509 (2011) 9271–9277.
[13] M.C. Navarro, M.C. Lagarrigue, J.M. Paoli, R.E. Carbonio, M.I. Gómez, J. Therm. Anal. Calorim. 102 (2009) 655–660.
[14] A. Chaudhuri, S. Mitra, M. Mandal, K. Mandal, J. Alloys Compd. 491 (2010) 703–706.
[15] M. Srivastava, A.K. Ojha, S. Chaubey, P.K. Sharma, A.C. Pandey, Mater. Sci. Eng. B 175 (2010) 14–21.
[16] M.S. Bernardo, T. Jardiel, M. Peiteado, A.C. Caballero, M. Villegas, J. Alloys Compd. 509 (2011) 7290–7296.
[17] A. Azam, A. Jawad, A.S. Ahmed, M. Chaman, A.H. Naqvi, J. Alloys Compd. 509 (2011) 2909–2913.
[18] M. Anis-ur-Rehman, M.A. Malik, M. Akram, K. Khan, A. Maqsood, Phys. Scripta 83 (2011) 015602.
[19] A. Ianculescu, F.P. Gheorghiu, P. Postolache, O. Oprea, L. Mitoseriu, J. Alloys Compd. 504 (2010) 420–426.
[20] T.N. Soitah, C. Yang, Curr. Appl. Phys. 10 (2010) 724–728.
[21] R.C. Kambale, P.A. Shaikh, C.H. Bhosale, K.Y. Rajpure, Y.D. Kolekar, J. Alloys Compd. 489 (2010) 310–315.
[22] S.S. Chougule, D.R. Patil, B.K. Chougule, J. Alloys Compd. 452 (2008) 205–209.
[23] Z. Dai, Y. Akishige, J. Phys. D: Appl. Phys. 43 (2010) 445403.
[24] G. Catalan, Appl. Phys. Lett. 88 (2006) 102902.
[25] S.T. Zhang, M.H. Lu, D. Wu, Y.F. Chen, N.B. Ming, Appl. Phys. Lett. 87 (2005) 262907.
[26] D.C. Jia, J.H. Xu, H. Ke, W. Wang, Y. Zhou, J. Eur. Ceram. Soc. 29 (2009) 3099–3103.
[27] M.M. Kumar, S. Srinath, G.S. Kumar, S.V. Suryanarayana, J. Magn. Magn. Mater. 188 (1998) 203–212.
[28] A.Z. Simões, F.G. Garcia, C.d.S. Riccardi, Mater Chem. Phys. 116 (2009) 305–309.